Nano Research
2022, 15(9): 7769–7777

ISSN 1998-0124 CN 11-5974/O4
https://doi.org/10.1007/s12274-022-4617-7

Research Article

Two-dimensional CoNi@mesoporous carbon composite with heterogeneous structure toward broadband microwave absorber

Yun Qiu[1], Haibo Yang[1] (✉), Fanfan Hu[2], and Ying Lin[1] (✉)

[1] *Shaanxi Key Laboratory of Green Preparation and Functionalization for Inorganic Materials, School of Materials Science and Engineering, Shaanxi University of Science and Technology, Xi'an 710021, China*
[2] *Jiangsu Product Quality Testing & Inspection Institute, Nanjing 210007, China*

Received: 6 April 2022 / **Revised:** 30 May 2022 / **Accepted:** 30 May 2022

ABSTRACT

Constructing composites with heterogeneous structure and dual loss mechanism shows great potential in designing microwave absorbers. In this work, two-dimensional cobalt and nickel alloys@mesoporous carbon (CoNi@MC) composites were constructed via using CoNi layered double hydroxide@mesoporous polydopamine (CoNi LDH@MPDA) as sacrifice template. During the pyrolysis process, the MPDA is transformed into mesoporous carbon coated the surface of CoNi LDH that is further reduced to CoNi alloys. The mesoporous structure is conducive to the multi-reflection of electromagnetic waves and facilitates optimizing impedance matching. Heterogeneous interfaces between CoNi alloys and mesoporous carbon induce interface polarization. Multiple attenuation mechanism promotes the electromagnetic waves conversion. The maximum reflection loss of CoNi@MC composite is −70.86 dB and the widest effective absorption bandwidth is 7.74 GHz covering almost the entire Ku band. This strategy will be a guidance for designing electromagnetic absorbers.

KEYWORDS

CoNi alloys, mesoporous carbon, microwave absorption, broad efficient frequency

1 Introduction

Nowadays, the widespread use of wireless communication technology and electronic equipment has resulted in severe electromagnetic radiation, which not only causes pollution to the environment but also harms human health [1, 2]. Reducing electromagnetic pollution is an inevitable requirement of the development of the times. At present, many efforts have been made to purify the electromagnetic environment [3–5]. Microwave absorption materials (MAMs) have great application value in the field of electromagnetic radiation protection and military stealth, which can transform incident electromagnetic waves into other forms of energy [6]. Traditional MAMs such as ferrite and $BaTiO_3$ always possess the shortcoming of narrow absorption bandwidth or high density, which severely limits their practical application [7–9]. Therefore, it is significant to develop novel and efficient absorbers with high attenuation intensity, lightweight, and wide frequency bandwidth [10–12].

Carbon materials have been widely used as MAMs because of their low cost, abundant resources, corrosion resistance, as well as strong dielectric loss [13–15]. Carbon with porous structure meets the requirements of lightweight MAMs and helps to increase the propagation path of microwave, thereby accomplishing the attenuation of electromagnetic waves [16, 17]. However, poor impedance matching seriously hinders its microwave absorption performance. Combining it with magnetic materials is an effective way to improve its performance, such as ferrite [18] and magnetic metal [19, 20]. Nano magnetic metal possessing the characteristics of high saturation magnetization and strong anisotropy is appealing, with increasing attention in microwave absorption field [21, 22]. Integrating magnetic metal with carbon can obtain MAMs with magnetic loss and dielectric loss, which will effectively improve the impedance matching of carbon.

Recently, a large number of studies have proved that controlling the microstructure for materials is of great significance to promote microwave energy conversion [23, 24]. Composites with hollow [25], core–shell [26], porous structure [27] always have high specific surface area, which not only introduces strong interfacial polarization but also reduces the filler loading. In particular, the porous structure reduces the impedance gap between the MAM and air, which finally enhances the effective absorption bandwidth (EAB). Thus, fabricating carbon with porous structure is another approach to balance the impedance matching and attenuation loss. However, preparation of porous carbon, especially with visible pores, usually requires silicon dioxide as a template and is removed by etching [28]. Utilizing simple method to synthesis carbon materials with porous structure is full of challenges.

Two-dimensional (2D) material has been widely used as MAMs because of the good process ability and low density [29]. Besides, the 2D materials always have thin thickness, which provides more opportunities for the penetration and dissipation of incident electromagnetic wave [30, 31]. Carbon with mesoporous and sheet structure will effectively combine the characteristics of 2D and porous structure, which is expected to be promising candidate for MAMs.

Herein, the 2D CoNi@MC composite is prepared by using

Address correspondence to Haibo Yang, yanghaibo@sust.edu.cn; Ying Lin, linying@sust.edu.cn

core–shell CoNi LDH@MPDA as precursor with a simple strategy. The heterogeneous structure of porous carbon and CoNi alloys enhances the interfacial polarization and multiple reflection. After pyrolysis, the shell of MPDA is transformed to nitrogen doped carbon that well inherits porous structure. Then, the core of CoNi LDH is reduced to metallic CoNi alloys. The abundant polarization, conduction loss, and magnetic loss endow the composite with superior microwave absorption performance. The optimal reflection loss (RL) reaches −70.86 dB and the EAB is 7.74 GHz, which is significantly better than that of CoNi@C composite without mesoporous structure. This work may pave a new way for tailoring materials with porous structure.

2 Experimental section

2.1 Reagents

Sinopharm Chemical Reagent Co., Ltd provided cobalt nitrate hexahydrate ($Co(NO_3)_2·6H_2O$), nickel nitrate hexahydrate ($Ni(NO_3)_2·6H_2O$), hexamethylene tetramine ($C_6H_{12}N_4$), 1,3,5-trimethylbenzene (TMB), and ammonia solution ($NH_3·H_2O$). Dopamine hydrochloride (DA) and triblock copolymer Pluronic F127 (F127) were purchased from Aladdin and Sigma-Aldrich, respectively. All the above reagents were used directly without further treatment.

2.2 Preparation of CoNi@MC composites

The CoNi LDH precursor was first fabricated according to the previous literatures with some modification [32, 33]. Firstly, 0.2 g of as-prepared CoNi LDH powder was dispersed in 20 mL mixed solution (ethanol:deionized water = 1:1). Then, 0.15 g of F127, 0.15 g of DA, and 0.5 mL of TMB were subsequently added under stirring. After half an hour, 0.4 mL $NH_3·H_2O$ was added to the above solution and kept stirring for 2 h. CoNi LDH@MPDA was collected by centrifugation. CoNi@MC composite was obtained by annealing the CoNi LDH@MPDA in Ar atmosphere with different temperature (600, 700, and 800 °C) for 2 h. The final products were named as CoNi@MC-600, CoNi@MC-700, and CoNi@MC-800, respectively, according to the different pyrolysis temperatures. In addition, the CoNi LDH@PDA composite without mesoporous structure was also synthesized for comparison. The preparation process was the same with CoNi LDH@MPDA without the addition of F127 and TMB. The final composite was labeled as CoNi@C-700 via pyrolysis CoNi LDH@PDA at 700 °C under Ar atmosphere.

2.3 Characterization

The phase structures of CoNi@MC composites were characterized by X-ray diffraction (XRD, D8 Advance, Germany) with the speed of 6 °/min and Raman spectrum (Raman, Renishaw Invia, England). The morphology was investigated by a scanning electron microscope (SEM, Hitachi, S-4800, Japan) and transmission electron microscope (TEM, FEI Tecnai G2 F20 S-TWIN, USA). The thermogravimetric (TG) analysis of CoNiLDH@MPDA was measured on thermogravimetric analyzer (SDT Q600, USA) under Ar atmosphere in the temperature range of (30–1,000 °C) with a heating rate of 10 °C/min. The X-ray photoelectron spectroscope (XPS, AXIS Supra, Kratos) was used to analyze valence and composition. Brunner–Emmet–Teller (BET, ASAP 2460, Micromeritics) was used to characterize the pore size distribution. The electromagnetic parameters of all the samples were measured on vector network analyzer (VNA, HP8720ES, Agilent, USA) via coaxial-line method. The CoNi@MC composite (20 wt.%) was uniformly mixed with paraffin (80 wt.%) and compressed into standard rings with inner and outer diameter of 3.04 and 7.00 mm, respectively.

3 Results and discussion

3.1 Structural and morphological analysis

The preparation process is presented in Scheme 1. First of all, CoNi LDH were prepared as template. Then, F127 and TMB molecules was used as soft template and mediator, respectively, to synthesis MPDA which coats on the surface of CoNi LDH. Finally, CoNi@MC composites with 2D heterogeneous structure was obtained by pyrolysis CoNi LDH@MPDA in Ar atmosphere.

The XRD patterns of precursors are displayed in Fig. 1(a), which shows pure CoNi LDH phase of CoNi LDH@PDA and CoNi LDH@MPDA precursors. Figure 1(b) exhibits the XRD pattern of CoNi@MC composites. The peaks of all samples at about 44°, 51°, and 76° correspond to (111), (200), and (220) planes of Co (JCPDS No. 15-0806) and Ni (JCPDS No. 14-0580), implying the formation of CoNi alloy [34]. It can be observed that the intensity of diffraction peaks for composite gradually increases as pyrolysis temperature increases, indicating that the crystallinity of CoNi is improved. When direct pyrolysis the CoNi LDH in Ar atmosphere at 700 °C, the obtained composite is consisted with CoO and Ni (Fig. 1(c)), suggestting that carbon plays an important role in the reduction of metal ions. TG curve of CoNi LDH@MPDA is presented in Fig. S1(a) in the Electronic Supplementary Material (ESM). It shows three weight loss stages. The first weight loss is ascribed to the evaporation of adsorbed water. The second weight loss (250–370 °C) is related to the decomposition of organic components. The third weight loss (370–600 °C) corresponds to the the combustion of partial carbon in order to the reduction of CoO. With the temperature increasing above 600 °C, the residual mass is almost unchanged. It implys that CoNi LDH@MPDA precursor hardly undergoes further thermal decomposition. Therefore, the carbonization temperature of CoNi LDH@MPDA is above 600 °C to ensure that organic part

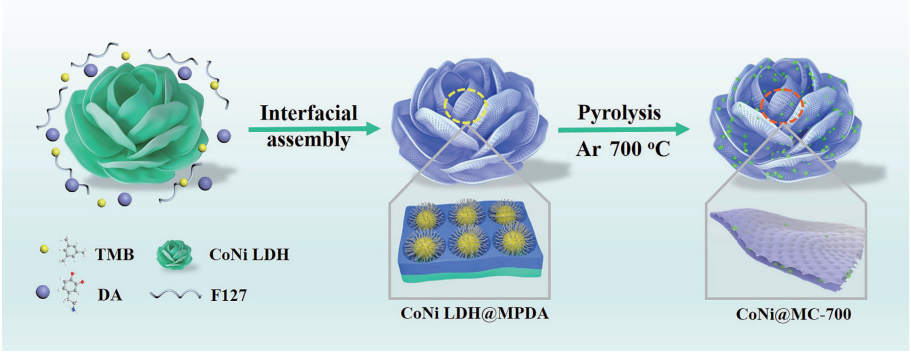

Scheme 1 Schematic illustration of preparing CoNi@MC composite.

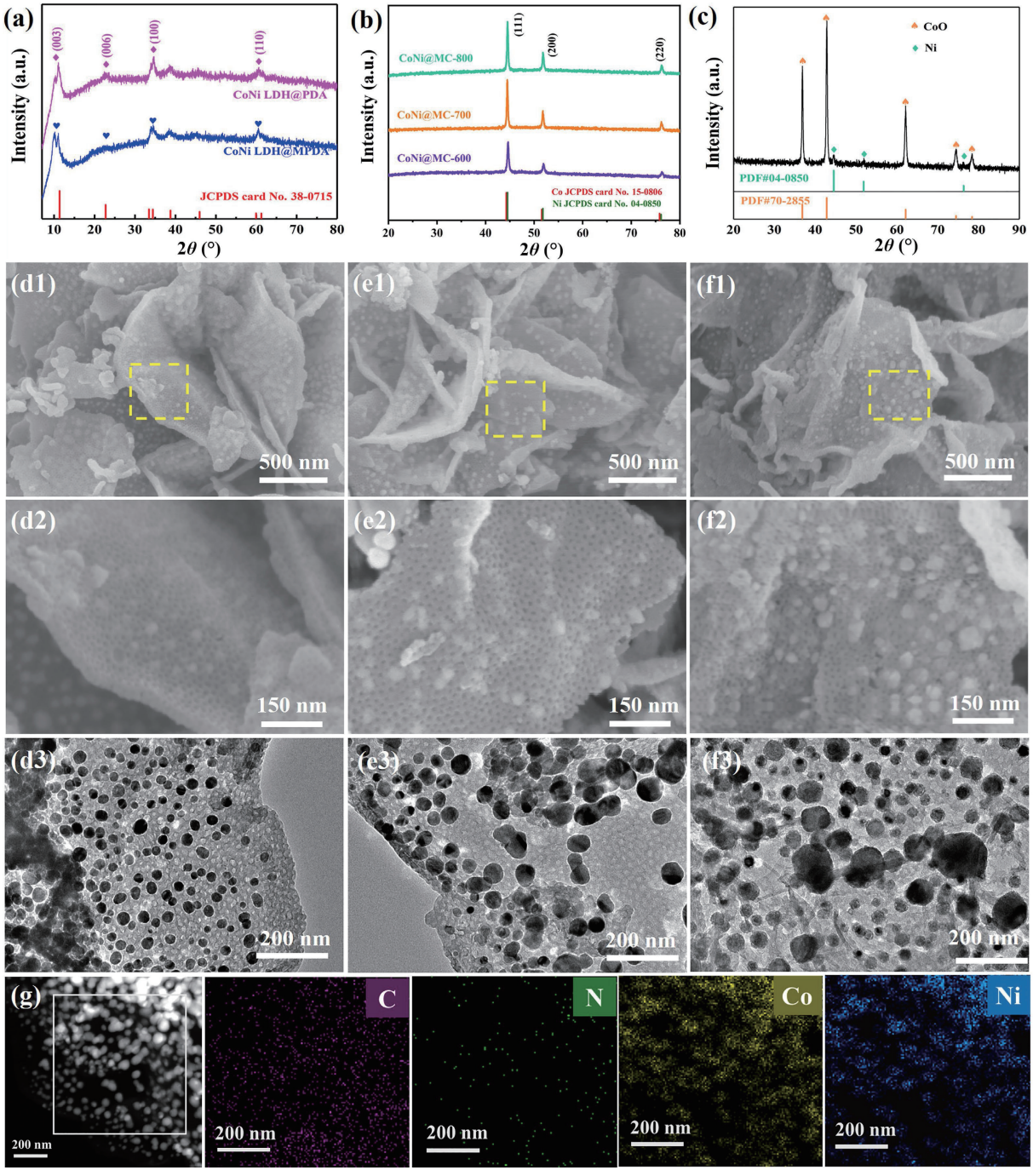

Figure 1 XRD patterns of (a) CoNi LDH@PDA and CoNi LDH@MPDA precursors, (b) CoNi@MC composites, and (c) pyrolyzed CoNi LDH, respectively. (d1)–(f1) low-magnification SEM images, (d2)–(f2) high-magnification SEM images, and (d3)–(f3) TEM images of CoNi@MC-600, CoNi@MC-700, and CoNi@MC-800 composites, respectively. (g) EDS mapping images of CoNi@MC-700 composite.

is fully carbonized.

Raman test was performed on CoNi@MC composites to verify the presence of carbon component, whose results are depicted in Fig. S1(b) in the ESM. It can be observed that all samples have peaks at about 1,360 and 1,590 cm^{-1}, which corresponds to the D and G bands, respectively [35]. The I_D/I_G values of CoNi@MC-600, CoNi@MC-700, and CoNi@MC-800 composite are 0.88, 0.92, and 0.93, respectively. The I_D/I_G values of CoNi@MC composites are lower than 1, indicating the higher graphitization degree of carbon component. It's worth noting that the graphitization degree of the composite is not increasing with the increase of the pyrolysis temperature. The reason for this phenomenon is that CoNi nanoparticles growing larger at high temperature damage the original lattice of carbon, leading to more defects for composites. Consequently, the CoNi@MC composite obtained at high pyrolysis temperature has more defects, which will enhance dipole polarization. At the same time, the uneven charge distribution will improve interface polarization.

The SEM images of CoNi LDH, CoNi LDH@PDA, and CoNi LDH@MPDA precursors are presented in Figs. S2(a)–S2(c) in the ESM. The CoNi LDH presents flower-like structure formed by self-assembly of 2D nanosheets (Fig. S2(a) in the ESM). As shown in Figs. S2(b) and S2(c) in the ESM, the surface of CoNi LDH@PDA precursor is smooth (Fig. S2(b) in the ESM), while the surface of CoNi LDH@MPDA precursor is rough (Fig. S2(c) in the ESM), because continuously open mesoporous PDA decorates the surface. The low-magnification SEM images of CoNi@MC-600, CoNi@MC-700, and CoNi@MC-800 are displayed in Figs. 1(d1)–1(f1). All the CoNi@MC composites present core–shell 2D sheet structure, whose shell is mesoporous carbon and the core is

nano-sized CoNi alloys. Figures 1(d2)–1(f2) show the high-magnification SEM images of CoNi@MC composites. It can be clearly observed that the surfaces of three samples are uniformly covered with apparently mesopores. When direct pyrolysis the CoNi LDH, the obtained particles consisted with CoO and Ni have large spaces between each other (Fig. S2(d) in the ESM). TEM images in Figs. 1(d3)–1(f3) further confirm that the outer carbon shell possesses mesoporous structure. Co^{2+} and Ni^{2+} in the CoNi LDH are reduced to CoNi nanoparticles during the pyrolysis process. The energy dispersive spectroscopy (EDS) elemental mapping images of CoNi@MC-700 composite are displayed in Fig. 1(g), confirming the coexistence of C, N, Co, and Ni elements. The out shell of mesoporous PDA well protects the morphology of CoNi LDH and alleviates the oxidation of CoNi alloys. For comparision, the CoNi@C-700 composite without mesoporous surface was also prepared. From SEM and TEM images of CoNi@C-700 in Figs. S2(e) and S2(f) in the ESM, it can be known that the surface of carbon is smooth and CoNi nanoparticles are not completely encased in carbon. In addition, the size of CoNi alloy gradually increases with the increase of pyrolysis temperature. The average particle sizes of CoNi alloy for CoNi@C-700, CoNi@MC-600, CoNi@MC-700, and CoNi@MC-800 are around 56, 25, 46, and 76 nm, severally, as presented in Figs. S3(a)–S3(d) in the ESM, which further verifies XRD result that the higher the pyrolysis temperature results in the stronger the crystallinity of the CoNi alloys.

N_2 adsorption–desorption tests were conducted on CoNi@MC composites to characterize their pore structure. It can be seen from Figs. 2(a)–2(c) that the N_2 adsorption–desorption isotherms is I-type, at the P/P_0 range of 0–0.1, implying the existence of micropores. When $P/P_0 > 0.1$, all CoNi@MC samples show typical IV-type N_2 adsorption–desorption isotherms companying with obvious H4 type hysteresis loop, which indicates the mesopore structure. Figures 2(d)–2(f) reveal the pore size distribution of CoNi@MC composites according to Barrett–Joyner–Halenda method. All the CoNi@MC composites present multi-scale pore structure. The average pore sizes of CoNi@MC-600, CoNi@MC-700, and CoNi@MC-800 are 18.9, 24.5, and 33.0 nm, respectively. The pores of the composites come from the interface between carbon and CoNi nanoparticles, and outer layer of mesoporous carbon. The porous structure is beneficial to reduce the density and realize the lightweight of MAM [36]. The heterogeneous interface of CoNi and carbon as well as mesoporous structure is advantageous to increase the attenuation path of electromagnetic wave and realize multiple scattering.

The XPS test of CoNi@MC-700 was carried out to analyze the surface chemical composition. Figure 2(g) displays the coexistence of C, N, O, Co, and Ni elements. In Fig. 2(h), five fitting peaks in C 1s spectra represent C–C, C=C, C–N, C–O, and O–C=O, respectively [37]. The N 1s spectra shown in Fig. 2(i) demonstrate the successful dope of the N element. Three peaks correspond to pyridinic N, pyrrolic N, and oxidized N, respectively [38]. The existence of N and O elements increases the defects in the carbon skeleton, thereby promoting the polarization of composite. The Ni 2p spectra consist with Ni $2p_{3/2}$, Ni $2p_{1/2}$, and satellite peaks, which confirms the coexistence of Ni^0 and Ni ions [39] (Fig. S4(a) in the ESM). The high-resolution spectra of Co 2p display several peaks. Two peaks at binding energy of 778.01 and 794.22 eV can be attributed to metal Co $2p_{3/2}$ and Co $2p_{1/2}$, respectively, while the other peaks represent the satellites indicating the existence of Co^{2+}

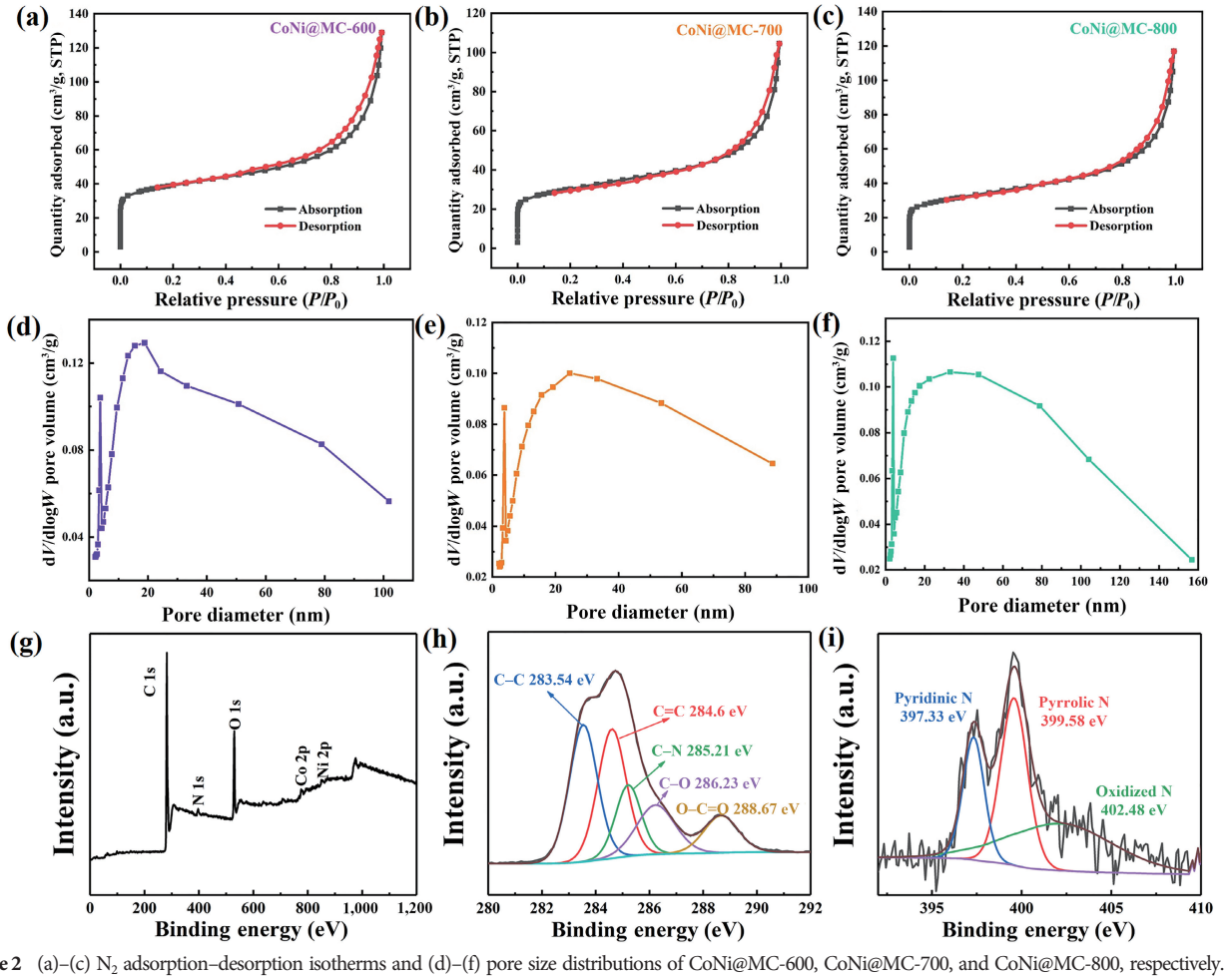

Figure 2 (a)–(c) N_2 adsorption–desorption isotherms and (d)–(f) pore size distributions of CoNi@MC-600, CoNi@MC-700, and CoNi@MC-800, respectively. XPS spectra of (g) survey spectrum, (h) C 1s, and (i) N 1s of CoNi@MC-700 composite.

and Co^{3+} [40], as displayed in Fig. S4(b) in the ESM.

Electromagnetic parameters ($\varepsilon_r = \varepsilon' - j\varepsilon''$, $\mu_r = \mu' - j\mu''$) are important factors affecting the absorbing properties of CoNi@C and CoNi@MC composites. The real and imaginary part represents the storage and consumption of electrical energy or magnetic energy capacity for materials, respectively [41]. In Figs. 3(a) and 3(b), ε'–f and ε''–f plots of all samples show similar trend, which decrease with the increasing of frequency. This is mainly caused by polarization relaxation. In the absence of external electromagnetic field, the dipole arrangement in the composite is haphazard. When the external electromagnetic field is applied, the dipole orientation in the composite will be adjusted from random to parallel to the external electromagnetic field, resulting in dipole polarization relaxation. However, in reality, this process is often accompanied by energy loss in order to overcome the resistance. With the gradually increase of frequency, the speed of dipole rearrangement cannot catch up with the change of applied electromagnetic field, and finally causes the phenomenon that the permittivity decreases with the increase of frequency [42]. The order of ε' and ε'' values for four samples is CoNi@MC-800 > CoNi@C-700 > CoNi@MC-700 > CoNi@MC-600. For CoNi@MC composites, it is found that the higher pyrolysis temperature leads to the increase of permittivity (ε' and ε''). The CoNi@MC composite synthesized at high temperature has better dielectric loss ability. At the same temperature, the permittivity of CoNi@C-700 is always greater than that of CoNi@MC-700 composite. According to Maxwell–Garnett theory, porous structure is beneficial to decrease the effective permittivity of material [37]. The mesoporous structure of CoNi@MC-700 composite provides more contact interface with air compared with CoNi@C-700 composite, which induces more interface polarization to dissipate microwave. Figure 3(e) exhibits the dielectric loss tangent ($\tan\delta_\varepsilon = \varepsilon''/\varepsilon'$) of four composites. The order of $\tan\delta_\varepsilon$ values for four samples is the same with that of ε' and ε'' values. Therefore, the increase of pyrolysis temperature will increase the electrical loss ability of composite. The CoNi alloys provide magnetic loss for composites. Figures 3(c) and 3(d) presents the relationship of permeability (μ' and μ'') values and frequency. The μ' and μ'' values of CoNi@C-700 and CoNi@MC composites fluctuate around 1 and 0, respectively. Moreover, some μ'' values of CoNi@MC-800 composite are below zero in the range of 9–18 GHz. The main reason for this phenomenon is that the motion of charges produces alternating electric field and further induces magnetic field. Then, the generated magnetic energy radiates out from the composite resulting in the negative value of μ''. The magnetic loss tangent ($\tan\delta_\mu = \mu''/\mu'$) is shown in Fig. 3(f). The $\tan\delta_\varepsilon$ values of samples are larger than $\tan\delta_\mu$ values, which reveals that the main loss mechanism in the electromagnetic absorption process is dielectric loss.

It is generally accepted that the dielectric loss primarily originates from polarization and conduction loss in the microwave frequency range. The polarization loss is mainly composed of

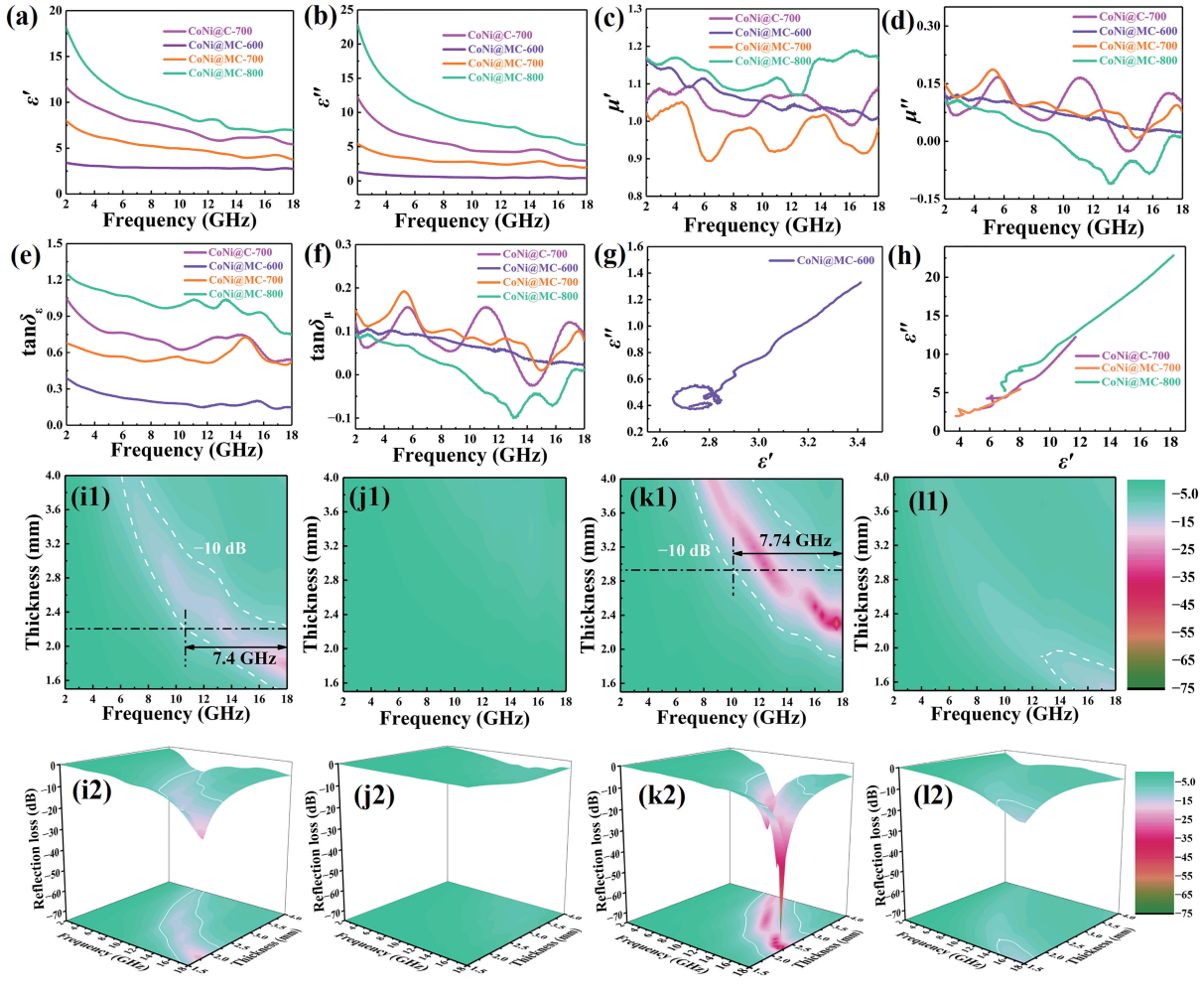

Figure 3 Frequency dependence of (a) ε', (b) ε'', (c) μ', (d) μ'', (e) $\tan\delta_\varepsilon$, and (f) $\tan\delta_\mu$ of CoNi@C-700, CoNi@MC-600, CoNi@MC-700, and CoNi@MC-800 composites, Cole–Cole curves of (g) CoNi@MC-600 and (h) CoNi@MC-700, CoNi@MC-800, and CoNi@C-700, (i1)–(l1) two-dimensional colour maps, and (i2)–(l2) three-dimensional RL diagrams of CoNi@C-700, CoNi@MC-600, CoNi@MC-700, and CoNi@MC-800 composites in the frequency range of 2–18 GHz.

interface polarization and dipole polarization. On the basis of Debye polarization equation, these polarization processes could be estimated by analyzing the relationship between ε' and ε'', as shown in Eq. (1) [43]

$$\left(\varepsilon' - \frac{\varepsilon_s + \varepsilon_\infty}{2}\right)^2 + \varepsilon''^2 = \left(\frac{\varepsilon_s - \varepsilon_\infty}{2}\right)^2 \quad (1)$$

where ε_s and ε_∞ are the static permittivity and the relative permittivity at infinite frequency, respectively. Single semicircle in ε'–ε'' curves represents one Debye relaxation process. Figures 3(g) and 3(h) display the ε' versus ε'' curves for four samples. In Cole–Cole plot, larger semicircle implies more significant polarization relaxation [41]. With the increase of pyrolysis temperature, the size of semicircles for corresponding CoNi@MC composite tunes to small, which signifies that the contribution of the Debye relaxation is weakened. The Cole–Cole plot of CoNi@MC-800 composite presents an approximately linear curve with weak semicircles, implying that the dominant form of dielectric loss is conduction loss [44]. The interfaces of carbon, CoNi nanoparticles, and air will accumulate many charges for introducing interface polarization. In addition, as concluded in XPS result, the existence of C–O, C=O, and nitrogen in CoNi@MC composites can act as polarization center of the dipole for inducing dipole polarization. Besides, the "tail" in Cole–Cole curve implays the contribution of conductive loss.

The magnetic loss provided by CoNi nanoparticles is also vital to determine the microwave absorption performance of composites. C_0 is used to represent the contribution of eddy current loss to magnetic loss on the basis of the following Eq. (2) [45]

$$C_0 = \mu''\mu'^{-2}f^{-1} \quad (2)$$

Figure S5(a) in the ESM presents the founctions of C_0 values for CoNi@C-700 and CoNi@MC composites with frequency. The C_0 values of four samples change obviously at 2–18 GHz, indicating that ferromagnetic resonance and eddy current loss are involved in the dissipation of incident electromagnetic energy.

According to the ε', ε'', μ', and μ'' values, the RL of composites can be calculated using transmission line theory based on the following Eqs. (3) and (4) [46, 47]

$$\mathrm{RL}\,(\mathrm{dB}) = 20\lg\left|\frac{Z_{in} - Z_0}{Z_{in} + Z_0}\right| \quad (3)$$

$$Z_{in} = Z_0\sqrt{\frac{\mu_r}{\varepsilon_r}}\tanh\left(\mathrm{j}\frac{2\pi fd}{c}\sqrt{\mu_r\varepsilon_r}\right) \quad (4)$$

where Z_{in} belongs to input impedance, Z_0 is the free space impedance, c represents the propagation speed of electromagnetic waves in vacuum, f represents the frequency of microwave, d is the thickness, respectively. Generally, when RL value is lower than −10 dB, 90% of the electromagnetic wave can be absorbed, the corresponding frequency range is regarded as EAB [48, 49]. Nowadays, higher requirements are put forward in practical applications for the effective absorption strength and EAB. Figures 3(i1)–3(l1) and Figs. 3(i2)–3(l2) display the two-dimensional colour maps (Figs. 3(i1)–3(l1)) and three-dimensional RL diagrams (Figs. 3(i2)–3(l2)) of four samples. The maxmium RL value of CoNi@C-700 composite is −16.29 dB at 2.0 mm. Further adjusting the thickness to 2.2 mm, the EAB reaches the widest to 7.4 GHz (Figs. 3(i1) and 3(i2)). As for CoNi@MC composites, CoNi@MC-700 exhibits the best microwave absorption performance.ThemaximumRLis−70.86dBwhenmatchingthicknessis 2.3 mm, and the corresponding EAB is 4.94 GHz. Moreover, when the matching thickness tunes to 2.9 mm, the broadest EAB of 7.74 GHz (10.2618 GHz) is achieved with RL value of −28.57 dB, as shown in Figs. 3(k1) and 3(k2). The CoNi@MC-600 and CoNi@MC-800 composites display poor microwave absorption performance. There is almost no electromagnetic absorption performance in CoNi@MC-600 composite whose RL values at different thickness are greater than −10 dB (Figs. 3(j1) and 3(j2)). The maximum RL value of CoNi@MC-800 composite is −13.95 dB and corresponding EAB is 2.82 GHz with thickness of 1.5 mm (Figs. 3(l1) and 3(l2)). Comparing the RL value and the maximum EAB of four composites, CoNi@MC-700 possesses the desirable electromagnetic wave absorption performance. Table 1 exhibits the recently reported comparison of the microwave absorption performance of carbon/magnetic metal composites [50–59]. The EAB, filler loading, and RL value further illustrate that CoNi@MC-700 is expected to become a candidate microwave absorber.

The above consequence implys that the heat treatment temperature and porous strucutre have no obvious influence on the magnetic loss strength and magnetic loss mechanism of CoNi

Table 1 Comparison of microwave absorbing properties among recently reported carbon/magnetic metal composites

Composites	Filler loading	Matching EAB (GHz)	RL_{max} (dB)	Thickness (mm)	References
Co/C	30 wt.%	4.6 (12.10–16.70)	−52.2	2.0	[50]
MXene-CNTs/Ni	30 wt.%	3.95 (6.00–9.95)	−56.4	2.4	[51]
Ni@C	25 wt.%	4.5 (13.50–18.00)	−59.8	1.5	[52]
MRBC-3	15 wt.%	5.77 (12.23–18.00)	−64.26	1.74	[53]
Co/NC	30 wt.%	5.75 (12.25–18.00)	−56.92	2.1	[54]
Ni/NiO/C	25 wt.%	5.67 (12.33–18.00)	−47.72	1.9	[55]
Ni/C	30 wt.%	4.40 (13.60–18.00)	−58.7	1.66	[56]
NC@NCNT	30 wt.%	5.20 (12.80–18.00)	−41.5	1.7	[57]
CoNi@NC/rGO	25 wt.%	6.70 (11.30–18.00)	−68	3.04	[58]
CNT-CoFe@C	10 wt.%	5.62 (12.38–18.00)	−40	3	[59]
CoNi/N-CNTs	30 wt.%	0.72 (2.80–3.52)	−52.64	3.8	[60]
Ni@NC-np	30 wt.%	6.25 (4.45–7, 14.3–18)	−52.88	7.2	[21]
CoNi@NCP-rGO	30 wt.%	4.03 (8.8–12.83)	−58.2	2.5	[44]
CoNi@MC-700	20 wt.%	7.74 (10.26–18.00)	−70.86	2.3	This work

alloys. The enhanced dielectric properties are the key to improve electromagnetic wave absorbing properties. It is known that attenuation capacity and impedance matching determine the microwave absorption performance of composites. The attenuation properties of the samples are evaluated by attenuation constants (α) [61]

$$\alpha = \frac{\sqrt{2}\pi f}{c}\sqrt{(\mu''\varepsilon'' - \mu'\varepsilon') + \sqrt{(\mu''\varepsilon'' - \mu'\varepsilon')^2 + (\mu'\varepsilon'' + \mu''\varepsilon')^2}} \quad (5)$$

Figure S5(b) in the ESM shows the attenuation constants of composites. Compared with CoNi@MC-600 and CoNi@MC-700, CoNi@MC-800 possesses the highest α values in the entire frequency range. Besides, the α values of CoNi@C-700 are bigger than these of CoNi@MC-700 composite. The order of α values for composites is consistent with that of dielectric loss. However, CoNi@C-700 and CoNi@MC-700 composites show comparable microwave absorption performance, which is unconsistent with the result of attenuation constant. Hence, the impedance matching is critical for influencing microwave absorption. Impedance matching can be represented by $|Z_{in}/Z_0|$ value. When $|Z_{in}/Z_0|$ value at the range of 0.8 to 1.2, better impedance matching characteristic can be obtained. Figure S5(c)–S5(f) in the ESM show the two-dimensional $|Z_{in}/Z_0|$ colour maps of four samples. The CoNi@MC-700 composite has the biggest frequency range with required $|Z_{in}/Z_0|$ values, manifesting its best impedence matching. Although CoNi@C-700 and CoNi@MC-800 have strong electromagnetic loss ability, the microwave absorption performance is not excellent because of its impedance mismatch. The mesoporous structure and suitable pyrolysis temperature are crucial to optimize the impedance matching of composite.

Figure 4 is schematic diagram of the electromagnetic wave absorption mechanism for CoNi@MC composite. Firstly, the combination of excellent impedance matching and appropriate attenuation ability attenuates most incident electromagnetic waves. Secondly, CoNi alloy and carbon endow composite with electrical conductivity. Magnetic NiCo alloys introduce magnetic loss mechanism such as ferromagnetic resonance and eddy current loss. The 2D CoNi@MC sheet forms conductive networks that helps electrons transmition. Thirdly, the incident microwave is reflected between the composites. The mesoporous structure on the surface promotes the scattering of electromagnetic waves. Then, after carbonization, organic part of CoNi LDH@MPDA precursor produces many defects and oxygen-containing groups that act as polarization sites generating dipole polarization. Moreover, heterogeneous structure of porous carbon and CoNi alloys facilitates the hopping and migration of electrons. Therefore, the synergistic effect of magnetic loss, conduction loss, and dielrctric loss contributes to the improvement of electromagnetic wave absorption performance.

4 Conclusion

In summary, 2D CoNi@MC composite was constructed by utilizing CoNi LDH@MPDA as precursor. The pyrolysis temperature and porous structure have important effects on microwave adsorption performance. The obtained CoNi@MC-700 composite displays excellent microwave attenuation ability. At the same pyrolysis condition, the prepared CoNi@C-700 composite without mesoporous structure shows weak absorbing properties. The mesoporous structure optimizes impedance matching resulting in the maximum reflection loss of −70.86 dB, and the broadest EAB of 7.74 GHz. This work supplies a valuable approach for the preparation of high efficiency carbon-based MAM with mesoporous structure.

Acknowledgements

This work was supported by the National Natural Science Foundation of China (No. 51772177), the Shaanxi Science & Technology Co-ordination & Innovation Project of China (No. 2017TSCXL-GY-08-05), and the Science Fund for Distinguished Young Scholars of Shaanxi Province (No. 2018JC-029).

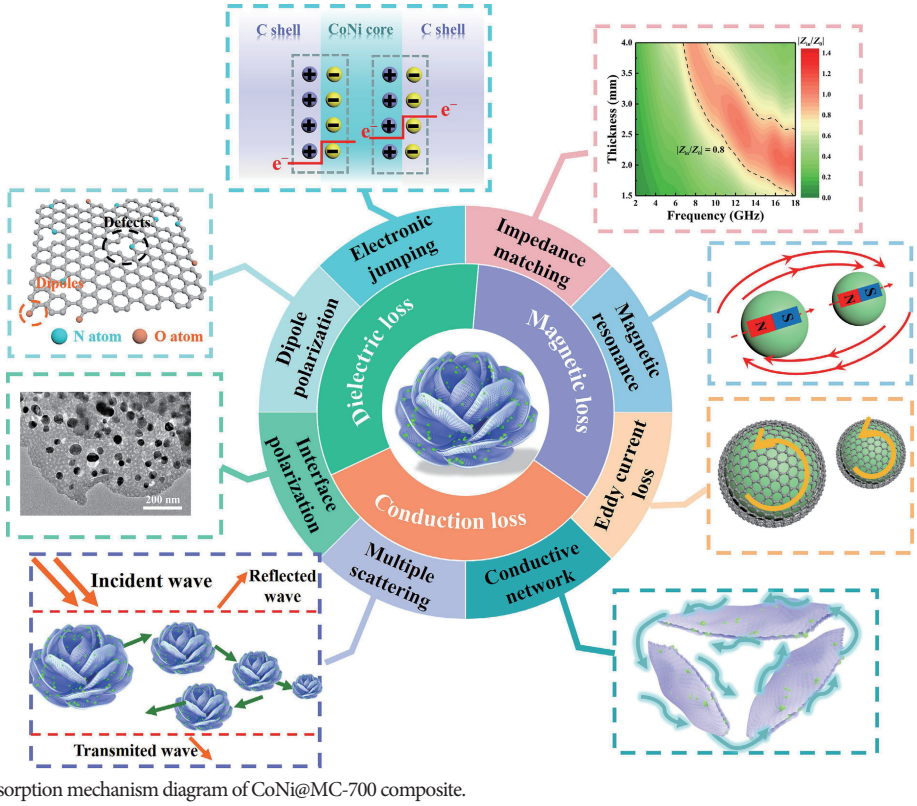

Figure 4 Microwave absorption mechanism diagram of CoNi@MC-700 composite.

Electronic Supplementary Material: Supplementary material (supplementary figures including the TG curve, Raman spectra, SEM images, average particle size distribution, XPS spectra, C_0 values, attenuation constant, and impedance matching characteristics) is available in the online version of this article at https://doi.org/10.1007/s12274-022-4617-7.

References

[1] Lv, H. L.; Yang, Z. H.; Wang, P. L.; Ji, G. B.; Song, J. Z.; Zheng, L. R.; Zeng, H. B.; Xu, Z. J. A voltage-boosting strategy enabling a low-frequency, flexible electromagnetic wave absorption device. *Adv. Mater.* **2018**, *30*, e1706343.

[2] Ma, T. B.; Ma, H.; Ruan, K. P.; Shi, X. T.; Qiu, H.; Gao, S. Y.; Gu, J. W. Thermally conductive poly(lactic acid) composites with superior electromagnetic shielding performances via 3D printing technology. *Chin. J. Polym. Sci.* **2022**, *40*, 248–255.

[3] Zhang, Y. L.; Ruan, K. P.; Gu, J. W. Flexible sandwich-structured electromagnetic interference shielding nanocomposite films with excellent thermal conductivities. *Small* **2021**, *17*, 2101951.

[4] Ma, Z. L.; Xiang, X. L.; Shao, L.; Zhang, Y. L.; Gu, J. W. Multifunctional wearable silver nanowire decorated leather nanocomposites for joule heating, electromagnetic interference shielding and piezoresistive sensing. *Angew. Chem., Int. Ed.* **2022**, *61*, e202200705.

[5] Han, Y. X.; Ruan, K. P.; Gu, J. W. Janus (BNNS/ANF)-(AgNWs/ANF) thermal conductivity composite films with superior electromagnetic interference shielding and Joule heating performances. *Nano Res.* **2022**, *15*, 4747–4755.

[6] Gou, G. J.; Meng, F. B.; Wang, H. G.; Jiang, M.; Wei, W.; Zhou, Z. W. Wheat straw-derived magnetic carbon foams: *In-situ* preparation and tunable high-performance microwave absorption. *Nano Res.* **2019**, *12*, 1423–1429.

[7] Saini, L.; Jani, R. K.; Janu, Y.; Kumar, M.; Patra, M. K.; Dixit, A. Gamma radiation induced microwave absorption properties of ultra-thin barium titanate (BaTiO3) ceramic tiles over X-band (8.2−12.4 GHz). *Ceram. Int.* **2021**, *47*, 22397–22403.

[8] Chen, X. L.; Wang, Y.; Liu, H. L.; Jin, S.; Wu, G. L. Interconnected magnetic carbon@$Ni_xCo_{1-x}Fe_2O_4$ nanospheres with core–shell structure: An efficient and thin electromagnetic wave absorber. *J. Colloid Interface. Sci.* **2022**, *606*, 526–536.

[9] Pan, J. L.; Guo, H. G.; Wang, M.; Yang, H.; Hu, H. W.; Liu, P.; Zhu, H. W. Shape anisotropic Fe_3O_4 nanotubes for efficient microwave absorption. *Nano Res.* **2020**, *13*, 621–629.

[10] Yan, J.; Huang, Y.; Zhang, X. Y.; Gong, X.; Chen, C.; Nie, G. D.; Liu, X. D.; Liu, P. B. MoS_2-decorated/integrated carbon fiber: Phase engineering well-regulated microwave absorber. *Nano-Micro Lett.* **2021**, *13*, 114.

[11] Xiang, Z.; Shi, Y. Y.; Zhu, X. J.; Cai, L.; Lu, W. Flexible and waterproof 2D/1D/0D construction of MXene-based nanocomposites for electromagnetic wave absorption, EMI shielding, and photothermal conversion. *Nano-Micro Lett.* **2021**, *13*, 150.

[12] Quan, B.; Gu, W. H.; Sheng, J. Q.; Lv, X. F.; Mao, Y. Y.; Liu, L.; Huang, X. G.; Tian, Z. J.; Ji, G. B. From intrinsic dielectric loss to geometry patterns: Dual-principles strategy for ultrabroad band microwave absorption. *Nano Res.* **2021**, *14*, 1495–1501.

[13] Wang, Y. Y.; Zhou, Z. H.; Zhou, C. G.; Sun, W. J.; Gao, J. F.; Dai, K.; Yan, D. X.; Li, Z. M. Lightweight and robust carbon nanotube/polyimide foam for efficient and heat-resistant electromagnetic interference shielding and microwave absorption. *ACS Appl. Mater. Interfaces.* **2020**, *12*, 8704–8712.

[14] Qiu, Y.; Yang, H. B.; Ma, L.; Lin, Y.; Zong, H. W.; Wen, B.; Bai, X. Y.; Wang, M. Q. *In situ*-derived carbon nanotube-decorated nitrogen-doped carbon-coated nickel hybrids from MOF/melamine for efficient electromagnetic wave absorption. *J. Colloid Interface. Sci.* **2021**, *581*, 783–793.

[15] Wang, L.; Ma, Z. L.; Zhang, Y. L.; Chen, L. X.; Cao, D. P.; Gu, J. W. Polymer-based EMI shielding composites with 3D conductive networks: A mini-review. *SusMat* **2021**, *1*, 413–431.

[16] Wang, Y. Y.; Zhou, Z. H.; Zhu, J. L.; Sun, W. J.; Yan, D. X.; Dai, K.; Li, Z. M. Low-temperature carbonized carbon nanotube/cellulose aerogel for efficient microwave absorption. *Compos. Part B:Eng.* **2021**, *220*, 108985.

[17] Zhao, Y. P.; Zuo, X. Q.; Guo, Y.; Huang, H.; Zhang, H.; Wang, T.; Wen, N. X.; Chen, H.; Cong, T. Z.; Muhammad, J. et al. Structural engineering of hierarchical aerogels comprised of multi-dimensional gradient carbon nanoarchitectures for highly efficient microwave absorption. *Nano-Micro Lett.* **2021**, *13*, 144.

[18] Zhang, Y. L.; Ma, Z. L.; Ruan, K. P.; Gu, J. W. Multifunctional $Ti_3C_2T_x$-(Fe_3O_4/polyimide) composite films with Janus structure for outstanding electromagnetic interference shielding and superior visual thermal management. *Nano Res.* **2022**, *15*, 5601–5609.

[19] Qiu, Y.; Lin, Y.; Yang, H. B.; Wang, L.; Wang, M. Q.; Wen, B. Hollow Ni/C microspheres derived from Ni-metal organic framework for electromagnetic wave absorption. *Chem Eng J.* **2020**, *383*, 123207.

[20] Xu, C. Y.; Wang, L.; Li, X.; Qian, X.; Wu, Z. C.; You, W. B.; Pei, K.; Qin, G.; Zeng, Q. W.; Yang, Z. Q. et al. Hierarchical magnetic network constructed by cofe nanoparticles suspended within "tubes on rods" matrix toward enhanced microwave absorption. *Nano-Micro Lett.* **2021**, *13*, 47.

[21] Jin, L. Q.; Yi, P. S.; Wan, L.; Hou, J. S.; Chen, P.; Zu, J. Q.; Wei, B.; Yao, Z. J.; Zhou, J. T. Thickness-controllable synthesis of MOF-derived Ni@N-doped carbon hexagonal nanoflakes with dielectric–magnetic synergy toward wideband electromagnetic wave absorption. *Chem. Eng. J.* **2022**, *427*, 130940.

[22] Tong, Z. Y.; Bi, Y. X.; Ma, M. L.; Liao, Z. J.; Huang, W. B.; Chung, K. L.; Ma, Y.; Wu, G. L.; Qu, Y. L; Pan, C. B. et al. Fabrication of flower-like surface Ni@Co_3O_4 nanowires anchored on RGO nanosheets for high-performance microwave absorption. *Appl. Surf. Sci.* **2021**, *565*, 150483.

[23] Shu, J. C.; Cao, W. Q.; Cao, M. S. Diverse metal-organic framework architectures for electromagnetic absorbers and shielding. *Adv. Funct. Mater.* **2021**, *31*, 2100470.

[24] Ge, J. W.; Cui, Y.; Qian, J. X.; Liu, L.; Meng, F. D.; Wang, F. H. Morphology-controlled CoNi/C hybrids with bifunctions of efficient anti-corrosion and microwave absorption. *J. Mater. Sci. Technol.* **2022**, *102*, 24–35.

[25] Qiu, Y.; Yang, H. B.; Cheng, Y.; Lin, Y. MOFs derived flower-like nickel and carbon composites with controllable structure toward efficient microwave absorption. *Compos. Part A-Appl. S.* **2022**, *154*, 10677.

[26] Wen, B.; Yang, H. B.; Lin, Y.; Ma, L.; Qiu, Y.; Hu, F. F.; Zheng, Y. N. Synthesis of core–shell Co@S-doped carbon@mesoporous N-doped carbon nanosheets with a hierarchically porous structure for strong electromagnetic wave absorption. *J. Mater. Chem. A* **2021**, *9*, 3567–3575.

[27] Qiu, Y.; Yang, H. B.; Cheng, Y.; Wen, B.; Lin, Y. Structure design of Prussian blue analogue derived CoFe@C composite with tunable microwave absorption performance. *Appl. Surf. Sci.* **2022**, *571*, 151334.

[28] Yu, Y. L.; Wang, M.; Bai, Y. Q.; Zhang, B.; An, L. L.; Zhang, J. Y.; Zhong, B. Tuning the inner hollow structure of lightweight amorphous carbon for enhanced microwave absorption. *Chem. Eng. J.* **2019**, *375*, 121914.

[29] Qiu, Y.; Yang, H. B.; Cheng, Y.; Bai, X. Y.; Wen, B.; Lin, Y. Constructing a nitrogen-doped carbon and nickel composite derived from a mixed ligand nickel-based a metal-organic framework toward adjustable microwave absorption. *Nanoscale* **2021**, *13*, 9204–9216.

[30] Pan, F.; Liu, Z. C.; Deng, B. W.; Dong, Y. Y.; Zhu, X. J.; Huang, C.; Lu, W. Lotus leaf-derived gradient hierarchical porous C/MoS_2 morphology genetic composites with wideband and tunable electromagnetic absorption performance. *Nano-Micro Lett.* **2021**, *13*, 43.

[31] Lv, H. L.; Zhou, X. D.; Wu, G. L.; Kara, U. I.; Wang, X. G. Engineering defects in 2D g-C_3N_4 for wideband, efficient electromagnetic absorption at elevated temperature. *J. Mater. Chem. A* **2021**, *9*, 19710–19718.

[32] Zhu, Y. Y.; An, S. L.; Sun, X. J.; Lan, D. W.; Cui, J. L.; Zhang, Y.

Q.; He, W. X. Core-branched $NiCo_2S_4$@CoNi-LDH heterostructure as advanced electrode with superior energy storage performance. *Chem. Eng. J.* **2020**, *383*, 123206.

[33] Lan, K.; Wei, Q. L.; Wang, R. C.; Xia, Y.; Tan, S. S.; Wang, Y. X.; Elzatahry, A.; Feng, P. Y.; Mai, L. Q.; Zhao, D. Y. Two-dimensional mesoporous heterostructure delivering superior pseudocapacitive sodium storage via bottom−up monomicelle assembly. *J. Am. Chem. Soc.* **2019**, *141*, 16755–16762.

[34] Li, C.; Qi, X. S.; Gong, X.; Peng, Q.; Chen, Y. L.; Xie, R.; Zhong, W. Magnetic–dielectric synergy and interfacial engineering to design yolk–shell structured CoNi@void@C and CoNi@void@C@MoS_2 nanocomposites with tunable and strong wideband microwave absorption. *Nano Res.* **2022**, *15*, 6761–6771.

[35] Wu, F.; Wan, L. Y.; Wang, T.; Tariq, M. R.; Shah, T.; Liu, P.; Zhang, Q. Y.; Zhang, B. L.; Construction of binary assembled MOF-derived nanocages with dual-band microwave absorbing properties. J. Mater. *Sci. Technol.* **2022**, *117*, 36–48.

[36] Xu, H.; Yin, X.; Zhu, M.; Han, M.; Hou, Z.; Li, X.; Zhang, L.; Cheng, L. Carbon hollow microspheres with a designable mesoporous shell for high-performance electromagnetic wave absorption. *ACS Appl. Mater. Interfaces.* **2017**, *9*, 6332–6341.

[37] Qiu, X.; Wang, L. X.; Zhu, H. L.; Guan, Y. K.; Zhang, Q. T. Lightweight and efficient microwave absorbing materials based on walnut shell-derived nano-porous carbon. *Nanoscale* **2017**, *9*, 7408–7418.

[38] Peng, L.; Peng, H. R.; Hung, C. T.; Guo, D. Y.; Duan, L. L.; Ma, B.; Liu, L. L.; Li, W.; Zhao, D. Y. Programmable synthesis of radially gradient-structured mesoporous carbon nanospheres with tunable core–shell architectures. *Chem* **2021**, *7*, 1020–1032.

[39] Liu, P. B.; Gao, S.; Wang, Y.; Zhou, F. T.; Huang, Y.; Huang, W. H.; Chang, N. H. Core–shell Ni@C encapsulated by N-doped carbon derived from nickel-organic polymer coordination composites with enhanced microwave absorption. *Carbon* **2020**, *170*, 503–516.

[40] Huang, W. H.; Zhang, X. X.; Zhao, Y. N.; Zhang, J.; Liu, P. B. Hollow N-doped carbon polyhedra embedded Co and Mo_2C nanoparticles for high-efficiency and wideband microwave absorption. *Carbon* **2020**, *167*, 19–30.

[41] Luo, J. H.; Feng, M. N.; Dai, Z. Y.; Jiang, C. Y.; Jiang, C. Y.; Yao, W.; Zhai, N. X. MoS_2 wrapped MOF-derived N-doped carbon nanocomposite with wideband electromagnetic wave absorption. *Nano Res.* **2022**, *15*, 5781–5789.

[42] Duan, Y. P.; Liu, Z.; Jing, H.; Zhang, Y. H.; Li, S. Q. Novel microwave dielectric response of Ni/Co-doped manganese dioxides and their microwave absorbing properties. *J. Mater. Chem.* **2012**, *22*, 18291–18299.

[43] Liu, Y.; Jia, Z. R.; Zhan, Q. Q.; Dong, Y. H.; Xu, Q, M.; Wu, G. L. Magnetic manganese-based composites with multiple loss mechanisms towards broadband absorption. *Nano Res.* **2022**, *15*, 5590–5600.

[44] Zhao, Y. Z.; Wang, W.; Wang, J. N.; Zhai, J. J.; Lei, X. Y.; Zhao, W.; Li, J. N.; Yang, H. W.; Tian, J. X.; Yan, J. F. Constructing multiple heterogeneous interfaces in the composite of bimetallic MOF-derivatives and rGO for excellent microwave absorption performance. *Carbon* **2021**, *173*, 1059–1072.

[45] Zhang, C. W.; Peng, Y.; Song, Y.; Li, J. J.; Yin, F. X.; Yuan, Y. Periodic three-dimensional nitrogen-doped mesoporous carbon spheres embedded with Co/Co_3O_4 nanoparticles toward microwave absorption. *ACS Appl. Mater. Inter.* **2020**, *12*, 24102–24111.

[46] Zhang, R. X.; Wang, L.; Xu, C. Y.; Liang, C. Y.; Liu, X. H.; Zhang, X. F.; Che, R. C. Vortex tuning magnetization configurations in porous Fe_3O_4 nanotube with wide microwave absorption frequency. *Nano Res.* **2022**, *15*, 6743–6750.

[47] Wang, Y. C.; Yao, L. H.; Zheng, Q.; Cao, M. S. Graphene-wrapped multiloculated nickel ferrite: A highly efficient electromagnetic attenuation material for microwave absorbing and green shielding. *Nano Res.* **2022**, *15*, 6751–6760.

[48] Wang, Y. Y.; Sun, W. J.; Lin, H.; Gao, P. P.; Gao, J. F.; Gai, K.; Yan, D. X.; Li, Z. M. Steric stabilizer-based promotion of uniform polyaniline shell for enhanced electromagnetic wave absorption of carbon nanotube/polyaniline hybrids. *Compos Part B-Eng.* **2020**, *199*, 108309.

[49] Liu, J.; Tao, L. L.; Gao, X. X.; He, X. X.; Wei, B.; Gu, Y. S.; Yao, Z. J.; Zhou, J. T. Morphology-size synergy strategy of SiC@C nanoparticles towards lightweight and efficient microwave absorption. *Chem. Eng. J.* **2022**, *433*, 134484.

[50] Pan, J. J.; Sun, X.; Jin, Z. Z.; Wang, T.; Zhao, Q. L.; Qu, H. J.; He, J. P. Constructing two-dimensional lamellar monometallic carbon nanocomposites by sodium chloride hard template for lightweight microwave scattering and absorption. *Compos. Pt. B-Eng.* **2022**, *228*, 109422.

[51] Li, X.; You, W. B.; Xu, C. Y.; Wang, L.; Yang, L. T.; Li, Y. S.; Che, R. C. 3D seed-germination-like mxene with *in situ* growing CNTs/Ni heterojunction for enhanced microwave absorption via polarization and magnetization. *Nano-Micro Lett.* **2021**, *13*, 157.

[52] Xiang, Z.; Zhang, X.; Shi, Y. Y.; Cai, L.; Cheng, J.; Jiang, H.; Zhu, X.; Dong, Y.; Lu, W. Efficient microwave absorption of MOFs derived laminated porous Ni@C nanocomposites with waterproof and infrared shielding versatility. *Carbon* **2021**, *185*, 477–490.

[53] Wei, B.; Zhou, C. Y.; Yao, Z. J.; Chen, P.; Wang, M. Q.; Li, Z. J.; Zhou, J. T.; Hou, J. S.; Li, W. Encapsulation of high specific surface area red blood cell-like mesoporous carbon spheres by magnetic nanoparticles: A new strategy to realize multiple electromagnetic wave loss mechanism. *Carbon* **2021**, *184*, 232–244.

[54] Tao, J. Q.; Xu, L. L.; Wan, L.; Hou, J. S.; Yi, P. S.; Chen, P.; Zhou, J. T.; Yao, Z. J. Cubic-like Co/NC composites derived from ZIF-67 with a dual control strategy of size and graphitization degree for microwave absorption. *Nanoscale* **2021**, *13*, 12896–12909.

[55] Lei, L.; Yao, Z. J.; Zhou, J. T.; Zheng, W. J.; Wei, B.; Zu, J. Q.; Yan, Y. K. Hydrangea-like Ni/NiO/C composites derived from metal-organic frameworks with superior microwave absorption. *Carbon* **2021**, *173*, 69–79.

[56] Li, J. J.; Zhang, F.; Lu, H. B.; Guo, W. B.; He, X. D.; Yuan, Y. Heterogeneous rod-like Ni@C composites toward strong and stable microwave absorption performance. *Carbon* **2021**, *181*, 358–369.

[57] Liu, D. W.; Du, Y. C.; Xu, P.; Wang, F. Y.; Wang, Y. H.; Cui, L. R.; Zhao, H. H.; J., H. X. Rationally designed hierarchical N-doped carbon nanotubes wrapping waxberry-like Ni@C microspheres for efficient microwave absorption. *J. Mater. Chem. A* **2021**, *9*, 5086–5096.

[58] Xu, X. Q.; Ran, F. T.; Fan, Z. M.; Cheng, Z. J.; Lv, T.; Shao, L.; Liu, Y. Y. Bimetallic metal-organic framework-derived pomegranate-like nanoclusters coupled with CoNi-doped graphene for strong wideband microwave absorption. *ACS Appl. Mater. Inter.* **2020**, *12*, 17882–17892.

[59] Wang, Y. Q.; Wang, H. G.; Ye, J. H.; Shi, L. Y.; Feng, X. Magnetic CoFe alloy@C nanocomposites derived from ZnCo-MOF for electromagnetic wave absorption. *Chem. Eng. J.* **2020**, *383*, 123096.

[60] Zhou, J.; Guo, F.; Luo, J. L.; Hao, G. Z.; Liu, G. G.; Hu, Y. B.; Zhang, G. P.; Guo, H.; Zhou, H.; Jiang, W. Designed 3D heterostructure with 0D/1D/2D hierarchy for low-frequency microwave absorption in the S-band. *J. Mater. Chem. C.* **2022**, *10*, 1470–1478.

[61] Di, X. C.; Wang, Y.; Fu, Y. Q.; Wu, X. M.; Wang, P. Wheat flour-derived nanoporous carbon@$ZnFe_2O_4$ hierarchical composite as an outstanding microwave absorber. *Carbon* **2021**, *173*, 174–184.